



# Carbon fabric coated with nanostructured zinc oxide layers for use in triboelectric self-powered touch sensors

S. I. Petrushenko<sup>1,2,4,\*</sup>, M. Fijalkowski<sup>2</sup>, V. R. Kopach<sup>3</sup>, Y. M. Shepotko<sup>3</sup>, K. Adach<sup>2</sup>, S. V. Dukarov<sup>1</sup>, V. M. Sukhov<sup>1</sup>, A. Fedonenko<sup>1</sup>, A. L. Khrypunova<sup>3</sup>, and N. P. Klochko<sup>3</sup>

<sup>1</sup>V.N. Karazin Kharkiv National University, 4, Svobody Square, Kharkiv 61022, Ukraine

<sup>2</sup>Technical University of Liberec, Studentska 2 str., 461 17 Liberec, Czech Republic

<sup>3</sup>National Technical University "Kharkiv Polytechnic Institute", 2, Kyrpychova str., Kharkiv 61002, Ukraine

<sup>4</sup>Faculty of Physics, V.N. Karazin Kharkiv National University, 4, Svobody Square, Kharkiv 61000, Ukraine

**Received:** 4 September 2023

**Accepted:** 12 February 2024

**Published online:**  
26 February 2024

© The Author(s), 2024

## ABSTRACT

An environmentally friendly, low-cost, and lightweight biocompatible textile triboelectric material was made by *in situ* coating carbon fabric (CF) with nanostructured zinc oxide (ZnO) layers using the automatic Successive Ionic Layer Adsorption and Reaction (SILAR) method. Depending on the deposition mode, we created triboelectric CF/ZnO textiles with multidirectionally intergrown short ZnO nanorods or with arrays of ZnO nanosheets. The Raman spectra confirmed the hexagonal wurtzite structure of both types of ZnO layers and the unique *a*-axis texture of the nanosheets. In the developed triboelectric CF/ZnO/PET/ITO sensors, the upper tribonegative part was made of a polyethylene terephthalate film coated with a thin layer of indium-tin oxide, and the lower tribopositive part was made of CF/ZnO textile. In tests with repeated hand tapping at low frequency 1.3–13 Hz and a force of ~ 5 N (pressure of ~ 33 kPa), the open-circuit voltage pulses were ~ 15 V for short ZnO nanorods and ~ 30 V for ZnO nanosheets, their duration did not exceed a few milliseconds. Due to the nanosheet morphology of the ZnO layer, the maximum touch-induced surface charge density for the corresponding triboelectric textile ( $0.7 \mu\text{C}/\text{m}^2$ ) was almost twice than for the CF/ZnO textile with intergrown ZnO short nanorods ( $0.4 \mu\text{C}/\text{m}^2$ ). The touch sensor with ZnO nanosheets showed an output voltage of 3.6 V, a current density of  $1.47 \mu\text{A}/\text{cm}^2$ , and a power density of  $1.8 \mu\text{W}/\text{cm}^2$ . It can be used as a dual-mode sensor due to ability to recognize the hardness of objects by analyzing the output current peaks.

Address correspondence to E-mail: petrushenko@karazin.ua; Serhii.Petrushenko@tul.cz

## 1 Introduction

With the rapid development of small electronics, including hundreds of billions of Internet of Things (IoT) devices, eco-friendly inexpensive and lightweight biocompatible power supplies and self-powered sensors that do not require recharging and replacement, are becoming more and more necessary. Among various power sources, the triboelectric nanogenerator (TENG) is distinguished in that it can harvest electrical energy for targeted applications from wasted mechanical energy in the environment through a combination of contact electrification and electrostatic induction [1–7]. There are various sources of mechanical energy for TENGs, as well as for self-powered triboelectric type sensors (triboelectric or TENG-based sensors, TESs), which can be used to convert into electricity, including voluntary and involuntary movements of the human body, sound, wind and water flow. For example, body motion and hand tapping can be applied to various industries such as robotics, health care, and sports, since TENG and TES generate electrical signals such as open-circuit voltage ( $UV_{oc}$ ), output voltage ( $UV$ ), and output current ( $I$ ), through an external load ( $R$ ) in response to mechanical touch, pressure, or movement of an object. The induced mechanical energy can be recognized via the amplitude and profile of the electrical output signals generated by the TES [2, 3, 5–7, 11, 12]. For example, the output amplitude  $UV_{oc}$  of the triboelectric sensor is strongly correlated with the contact pressure, so that the contact pressure can be estimated from the output amplitude of the TES. In addition, the position, trajectory and speed of a moving object, as well as its mechanical hardness, can be estimated from the profile of the output current signals from the array of triboelectric sensors [2, 5–7, 11, 12].

Recently, wearable triboelectric nanogenerators and TENG-based sensors containing fibers, yarns and textiles have received intense attention as they combine the functions of energy harvesters and self-powered sensors with the advantages of flexibility, which is vital for rapid progress in smart textiles and IoT wearable electronics [3–11]. According to [4, 11, 12], textile TENGs and TESs show scalable potential and better incorporation with clothes as stacking layer structures, showing advantages in scalability and electricity output. They are applied in both wearable power sources and human-interactive sensors, such as human motion and physiological sensing, multifunctional pressure

sensing electronic skin, and human respiratory monitoring, promising for human healthcare and biomedical applications. In addition, textile TENGs and TESs are the fundamental basis of self-charging wearable systems, such as the self-powered human-machine interactive keyboard for applications in biometrics described in [7, 12]. According to [7, 12], the self-powered wearable keyboard, has been fabricated by integrating large-area textile TES arrays, not only can track and record electrophysiological signals, but can also identify individuals' typing characteristics. The developed keyboard, as well as various TENG-based touch and pressure sensors described in [7, 12], have promising applications in wearable electronics, cybersecurity, and artificial intelligence. It should be emphasized that textile TENG and TES can be mass-produced and are best combined with clothing in the form of layered structures [4, 10–12]. An important advantage of triboelectric devices, and in particular textile triboelectric sensors, is a wide choice of available materials, environmental friendliness and low-cost manufacturing technologies [2, 10, 11]. The most promising is the production TENGs and TESs through in situ functionalization of ready-made textiles woven from synthetic or natural fibers/yarns [4], since this approach can provide a wider choice of materials and highly efficient fabrication of scalable textile triboelectric devices. Since in situ functionalization is free from size restrictions of the target textile, which allows the creation of easy-to-use, inexpensive and mass-produced "smart textiles" [4], this approach was successfully used in [3–8] for applying triboelectric layers to the surface of fabrics.

The operation of TENG and TES, including the most common contact-separating mode, is based on the contact electrification of triboelectric layers, when the surface of a material with a higher electron affinity is charged negatively, and the other surface is positively charged. According to [2, 9, 10], modification of the surface morphology of triboelectric layers can increase the area of friction or contact; therefore, it is considered as one of the main ways to improve the output characteristics of TENGs and TESs. As a result of triboelectrification and subsequent electrostatic induction, excess electrons are transferred from electrodes connected to triboelectric materials to an external circuit. Thus, there is a crucial need for reliable conductive electrode materials, which is a problem for textile triboelectric devices [9, 10, 12]. Usually, a metallization of natural and synthetic fabrics, such as

cotton, nylon, acrylic and polyester, with copper [5, 9, 10], zinc [10], aluminum [5, 9, 12], gold [9, 12], nickel [9, 10, 12], platinum [12] or silver [2, 3, 7–9, 12] were used to obtain conductive electrodes in textile TENGs and TEs. Typically, metals in the form of sheets or as coatings on the surface of commercial fabrics were obtained by sputtering, evaporation or electroless plating. Metal coated fabrics have also been produced by ink-printing and dip-coating using solutions of metal nanoparticles and nanowires. Similarly, polymeric textile electrodes have been produced using conductive organic materials such as polyacetylene, polypyrrole, and polystyrene sulfonate (PEDOT:PSS) [12]. However, according to [12], metallic (except noble metals) and polymeric electrode materials are easily oxidized and become unstable in a humid environment, so that their conductivity decreases with time. In addition, they easily fall off the fabric, and this is unsafe for the environment and the human body. According to [9, 12], a good choice is to use carbon-based coatings to cover the surface of ordinary fabric for the manufacture of conductive electrodes for TENGs and TEs. Carbon materials such as carbon nanotubes, carbon black, and graphene nanosheets have high electrical conductivity, good plasticity, and degradability. However, despite the fact that such carbon-coated fabrics have many advantages, they cannot be widely used due to the difficulty of their processing [12]. At the same time, commercial carbon fabric (CF) is mechanically and chemically resistant, like other fabrics, but it uses conductive carbon fibers instead of more traditional threads such as cotton or polyester. Therefore, as a part of TENG, carbon fabric does not need a metal coating or other conductive coatings. This makes it possible to insert a textile triboelectric device into certain places in ordinary clothing and connect conductive carbon fibers to an external electrical load [13].

In this work we present new triboelectric textile material based on a conductive commercial woven carbon fabric, whose fibers were in situ functionalized with nanostructured zinc oxide (ZnO) layers. To date, various ZnO nanostructures are widely integrated into TENGs and self-powered TENG-based sensors due to the inherent piezoelectric properties and excellent electromechanical properties of zinc oxide [2, 4, 6, 12, 14]. In [6], the pressure measurement mechanism of touch TEs with nanostructured ZnO layers was explained by the effect of enhanced triboelectric-piezoelectric coupling. Modulation of growth ZnO nanostructures for the maximum output power of a hybrid

piezo/triboelectric nanogenerator was studied in [14]. Recently, the use of ZnO in TENGs based on polymer composites [2, 8, 12] and in various textile TENGs [4, 6] was reported. Namely, the authors of [6] described a self-powered TENG-based sensor consisting of chemically grown zinc oxide nanorods on a textile cotton platform, and its effectiveness was confirmed when attached to the human body. Regarding arrays of zinc oxide nanostructures on the surface of carbon fibers, the following recent information is available. In [15], ZnO nanoarrays fabricated on carbon fibers using combined atomic layer deposition and hydrothermal methods showed excellent piezoelectric properties. ZnO nanowires on the surface of carbon fiber obtained by hydrothermal synthesis in [16] were used as friction materials with improved friction and wear resistance. ZnO nanoflowers grown on CF using a simple hydrothermal process made it possible to obtain a highly efficient supercapacitor electrode in [17]. In [18], carbon fibers covered with ZnO nanowires were used as a functional material CF/ZnO for an efficient hybrid piezoelectric nanogenerator. The CF/ZnO in [18] was synthesized by a two-stage procedure, which includes the deposition of ZnO seed layers by the dip-coating method and the hydrothermal synthesis of zinc oxide nanowires on the surface of the carbon fabric. The authors of [19] fabricated arrays of ZnO nanorods on carbon fabric in a similar way in order to construct multiscale reinforcement of the friction material. The chemical bond (C–O–Zn) between the ZnO nanostructure and the carbon fiber ensured a high and stable coefficient of friction. In [19], the use of CF/ZnO fabric as a matrix in a multilayer polymer composite made it possible to manufacture products with improved mechanical properties and outstanding tribological characteristics used for transmission and braking systems of vehicles. Thus, our approach, which consists in using CF to create a triboelectric CF/ZnO material based on nanostructured zinc oxide layers for use in TENG-based self-powered sensors, is quite promising and, at the same time, innovative.

Herein, for the in situ functionalization of the carbon fabric, we used two modes of growing nanostructured ZnO arrays using the automatic Successive Ionic Layer Adsorption and Reaction (SILAR) method. Depending on the deposition mode, the automatic SILAR method made it possible to create CF/ZnO materials differing from each other in the morphology and composition of nanostructured ZnO layers. As a proof-of-concept, we developed and tested two

prototype TENG-based sensors: one with multidirectionally intergrown short ZnO nanorods, and the second with arrays of ZnO nanosheets, combining the advantages of autonomy, availability of materials, simplicity of design, low-cost, and ease of manufacture, and compared their output characteristics.

## 2 Experimental details

To create a CF/ZnO textile triboelectric material, we used the in situ coating of a plain woven carbon fabric (Havel COMPOSITES CZ Ltd) with nanostructured zinc oxide layers using the automatic SILAR method. All chemicals used for this were of analytical grade. Pieces of carbon fabric with an active area of  $2.5 \times 5$  cm each were used as substrates. They were cleaned

by soaking overnight in a 10% aqueous solution prepared by diluting Elma lab clean A20sf (ELC A20sf) surfactant-free cleaning concentrate. Then, the CF substrates were sequentially washed in a flow of distilled water, acetone, and ethanol. After that, some experimental samples (CF/ZnO-1 and CF/ZnO-2) were fabricated by the SILAR method on the surface of CF fibers pre-coated with ZnO seed layers, and other samples (CF/ZnO-3 and CF/ZnO-4) were prepared by a similar SILAR method, but using bare carbon fabrics. A schematic representation of the process of manufacturing triboelectric textiles is shown in Fig. 1.

To prepare the ZnO seed layer by the dip-coating method, we immersed the CF sample for 30 s in an aqueous solution with a tetraamine-zinc complex  $[\text{Zn}(\text{NH}_3)_4]^{2+}$ , obtained by dissolving 0.05 M ZnO in an ammonia solution ( $\text{NH}_4\text{OH}$ ) up to pH 10.3. Then the

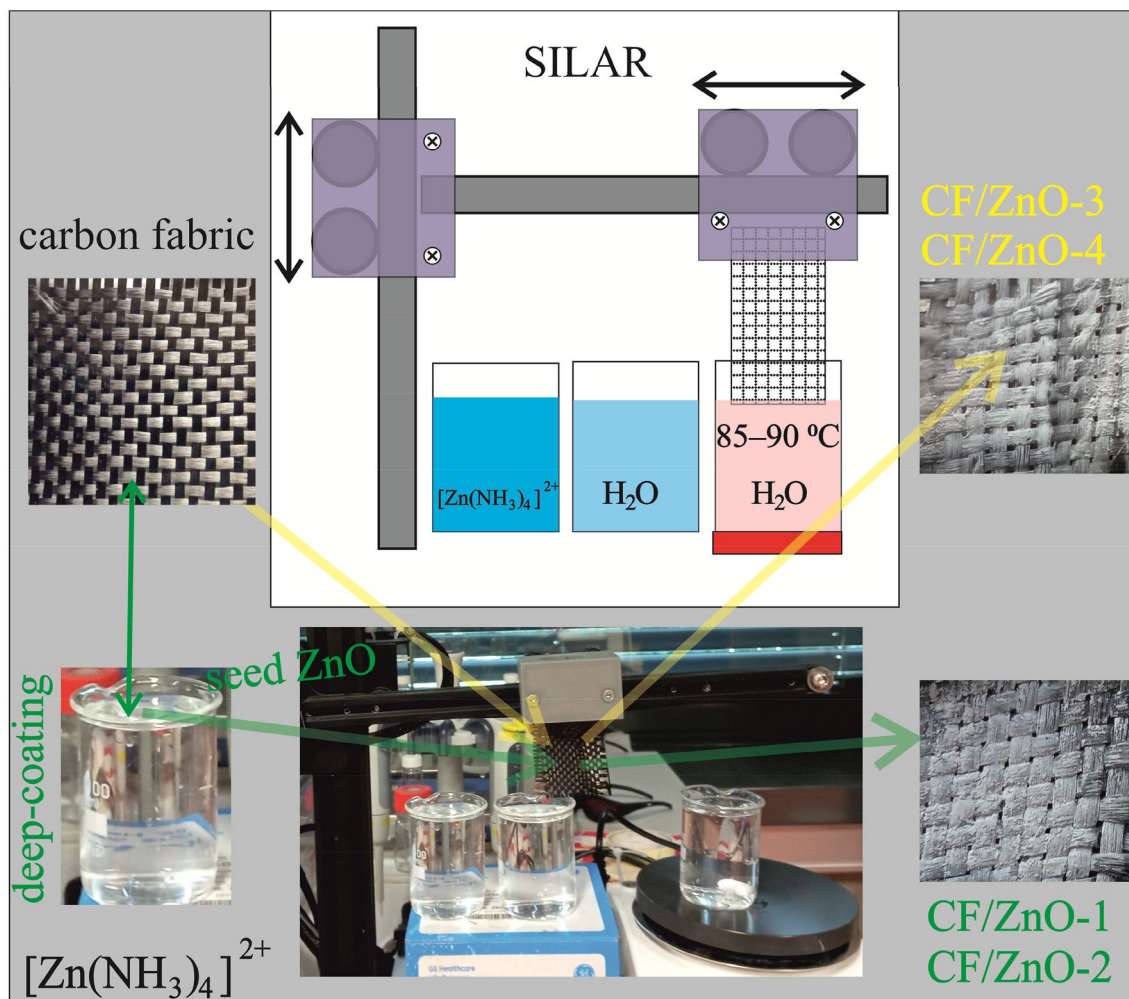


**Fig. 1** Schematic of the process of manufacturing triboelectric textiles by applying nanostructured ZnO films on carbon fabric by the automatic SILAR method with and without preliminary coating of seed layers



CF substrate was dried in a hot air flow. This process was repeated 10 times to obtain a ZnO seed layer that evenly coated the carbon fibers.

To deposit a nanostructured ZnO film on a carbon fabric by the SILAR method, an aqueous solution of zinc sulfate (1 M ZnSO<sub>4</sub>) and NH<sub>4</sub>OH was used as a cationic precursor. The cationic precursor was prepared by slowly adding 25% NH<sub>4</sub>OH to the ZnSO<sub>4</sub> solution. Initially, a precipitate of Zn(OH)<sub>2</sub> was formed, but in an excess of ammonia (at pH 12.1) it turned into a colorless transparent solution containing the tetraamine-zinc complex [Zn(NH<sub>3</sub>)<sub>4</sub>]<sup>2+</sup>. Hot (85–90 °C) distilled water was used as an anionic precursor in the SILAR process. To achieve good reproducibility of the deposition process and ensure the scalability of the SILAR method, its automation was applied on the basis of a universal motorized platform with numerical control (CNC), a photograph of which is shown in Fig. 1. Such platforms are widely used in conventional commercial 3D printers. All stages of the SILAR method were programmed using the g-code and the reproducibility of the carbon fiber immersion rate and the time of each deposition stage was ensured with an error of <0.1%. In the SILAR deposition process, one growth cycle included the following three stages. The first stage consisted in immersing the CF substrate in a solution of the [Zn(NH<sub>3</sub>)<sub>4</sub>]<sup>2+</sup> cationic precursor for 10 s. The second stage was its immersing in a hot distilled water agitated with a magnetic stirrer at 100 rpm for 10 s. The third stage was its rinsing in distilled water at room temperature for 5 s to remove excess ions and weakly bound particles from the surface. For 25 cycles of SILAR, experimental samples of triboelectric textiles CF/ZnO-1, CF/ZnO-2, CF/ZnO-3 and CF/ZnO-4 were obtained, photos of which are shown in Fig. 1.

The morphology of triboelectric textiles, as well as the surface of bare CF, was studied using scanning electron microscopy (SEM) images obtained in the secondary electron mode on a TESCAN Vega3 SBU scanning electron microscope operating at an accelerating voltage of 30 kV. In addition, SEM images and energy-dispersive X-ray (EDS) spectra were obtained using a Zeiss ULTRA Plus SEM instrument with in-lens secondary electron detector objective equipped with an OXFORD X-Max 20 EDS detector. The EDS spectra for the analysis of the elemental composition of the samples were recorded from their sections with a size of about 50 × 50 μm at an accelerating voltage of 10 kV. In addition, we combined the imaging capabilities of

the SEM with X-ray EDS measurements to create EDS maps.

Raman spectroscopy, as an optical method based on inelastic scattering of monochromatic light, was used for qualitative and quantitative studies of electron-phonon interaction in the nanostructured ZnO films of triboelectric textiles, since it is sensitive to crystal lattice distortions, crystal defects, and phase transformations [19–26]. The vibrational phonon modes of nanostructured ZnO layers deposited via SILAR method on surface of carbon fabric were characterized using a Raman microscope (Thermofisher Nicolet DXR Microscope) with solid-state diode green laser having excitation wavelength 532 nm and power 10 mW. The Raman spectra were obtained at room temperature in the backscattering geometry; they reflected multidirectional scattering of phonons from a laser spot ~2.1 μm in size. The Raman signal was integrated over 1 s exposure with 100 exposures for each sample. Signal intensity, peak width (namely, full width at half maximum, FWHM) and position (Raman shift frequency) were used as a measure of the crystal quality of ZnO. In the analysis, it was taken into account that thin films show slightly different spectra than bulk material, which can be correlated with uncontrolled propagation of light [26]. Moreover, it was assumed that not only the crystalline disorder of as-grown ZnO layers deposited on the carbon fabric by the SILAR method, but also local heating under the action of the laser beam can cause a shift and broadening of the Raman peaks, as well as a change in their intensity.

The spectra of diffuse reflectance  $R_d(\lambda)$  from the surfaces of CF and triboelectric textiles were studied on a LAMBDA 35 PerkinElmer spectrophotometer in the wavelength  $\lambda$  range 200–1100 nm. In accordance with [27], optical band gap ( $E_g$ ) for direct allowed transitions in ZnO films was determined using the Kubelka-Munk function  $F(R_d)$ :

$$F(R_d) = \frac{(1 - R_d)^2}{2R_d} \quad (1)$$

According to [27],  $E_g$  of ZnO was determined from the graph  $(F(R_d) \cdot hv)^2$  vs.  $hv$  by extrapolating its linear part on  $hv$ .

In this work, a prototype of a flexible wearable TENG-based touch sensor was developed and tested as a proof-of-concept consisting in the use of triboelectric textiles with nanostructured zinc oxide films deposited by the SILAR method on fibers of the

electrically conductive carbon fabric acting as an electrode. The design of the developed touch TES of the most common mode of vertical contact-separation is schematically shown in Fig. 2a. In this TENG-based touch sensor, the upper tribonegative part is made of a flexible thin-film polyethylene terephthalate (PET) plate with high electron affinity, coated with a conductive layer of indium-tin oxide (ITO) that acts as top electrode. Here we used a commercial PET/ITO tape from MSE Supplies LLC, in which a 175  $\mu\text{m}$  thick PET film is coated with a thin layer of ITO with a sheet resistance of 6–10  $\Omega/\text{sq}$ . Its SEM image is shown in Fig. 2a at the top. The tribopositive part of the sensor is made of textile CF/ZnO, its low magnification SEM image is shown in Fig. 2a at the bottom. A feature of the design of this TENG-based sensor of the vertical contact-separation mode with the double-electrode configuration is its simplicity due to the absence of a specially designed spacer that provides an air gap between the upper and lower triboelectric layers. This gap is typical for TENG and TES of such mode [1–3, 5, 6, 9, 28, 29]. According to [1, 30], when an external compressive force is applied, two nonconductive layers come into contact with each other. Then, in the area of contact, the surface charge is transferred by triboelectrification, and due to electrostatic induction, the electrodes become oppositely charged. If we take the electrical potential of the top electrode as zero, the

electrical potential  $UV$  of the bottom electrode can be calculated by the formula [1, 30]:

$$V = \frac{\sigma d}{\epsilon_0} \quad (2)$$

where  $\sigma$  is the triboelectric charge density,  $\epsilon_0$  is the vacuum permittivity, and  $d$  is the interlayer distance at a given state.

If, instead of an air gap, a spacer made of an elastic material with a relative permittivity  $\epsilon$  is used, then dependence (2) is transformed according to [14] into:

$$V = \frac{\sigma d}{\epsilon_0 \epsilon} \quad (3)$$

However, as has been recently confirmed [31], an air gap between triboelectric materials is not needed if one triboelectric layer is elastic and has a surface with a hemispherical matrix structure that can be deformed to create a planar contact with the opposite triboelectric layer. The area of this contact depends on the applied compressive force and allows the separation of triboelectric charges to charge opposite electrodes by electrostatic induction. Since the structure of the hemisphere array functions as a spring keeping the upper and lower materials separate, an efficient no-spacer TENG-based pressure sensor has been successfully developed and tested [31]. Similarly, the all-fabric

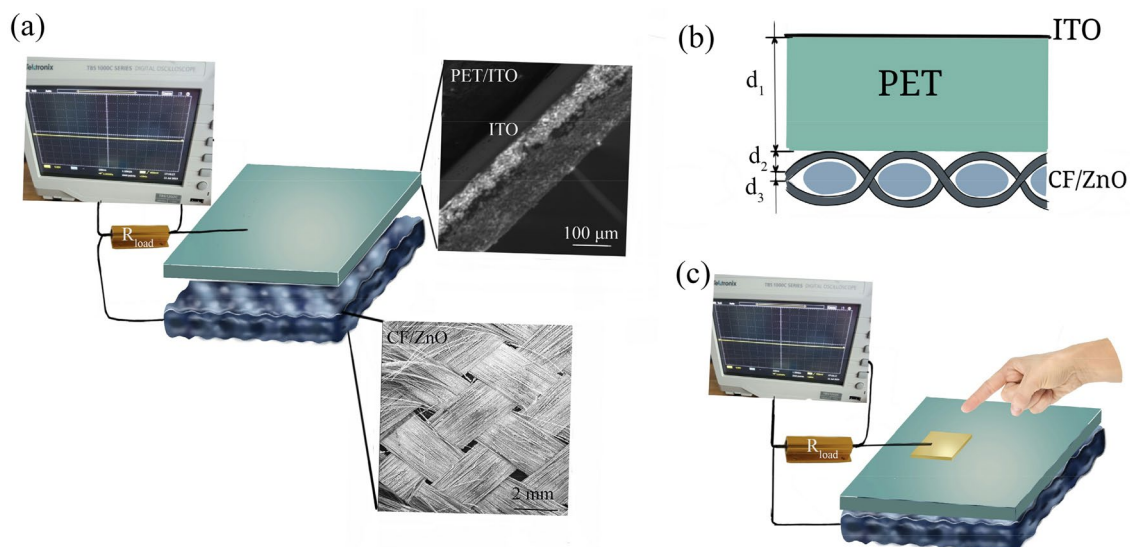


**Fig. 2** **a** Schematic of the flexible wearable TENG-based touch sensor with a CF/ZnO/PET/ITO composition and SEM images of top electronegative triboelectric part PET/ITO and bottom electropositive triboelectric part CF/ZnO. **b** Cross-sectional diagram

of a section of this sensor. **c** Schematic of testing the flexible wearable TENG-based touch sensor with the CF/ZnO/PET/ITO composition made in this work

triboelectric nanogenerators presented in [7], which function as self-powered interactive human-machine keyboards, also do not have specially designed separators or springs between the triboelectric layers due to such textile-specific advantages as high surface roughness and elasticity. As shown schematically in Fig. 2b, in the sensor developed by us, a gap is involuntarily formed between a smooth PET layer of thickness  $d_1$  and a woven textile coated with a nanostructured ZnO film of thickness  $d_2$ , with an average height of fabric irregularities  $d_3$  equal to 150  $\mu\text{m}$ . According to [1, 5, 32, 34], the maximum-induced surface charge density  $\sigma_m$  for each triboelectric layer equals:

$$\sigma_m = \frac{\sigma d_3 \epsilon_{\text{PET}} \epsilon_{\text{ZnO}}}{d_1 \epsilon_{\text{ZnO}} + d_3 \epsilon_{\text{PET}} \epsilon_{\text{ZnO}} + d_2 \epsilon_{\text{PET}}} \quad (4)$$

where the relative permittivity of PET is  $\epsilon_{\text{PET}} \approx 3.4$  and the relative permittivity of the nanostructured ZnO layer is  $\epsilon_{\text{ZnO}} \approx 17$  [33].

Fig. 2c schematically shows the testing process of the prototype of a flexible wearable TENG-based touch sensor with a CF/ZnO/PET/ITO composition fabricated in this work. For testing, we used a digital oscilloscope TBS 1202C Tektronix and connected in

series to the touch sensor electrical loads with resistances  $R_{\text{of}}$  of 0.27 M $\Omega$ , 0.62 M $\Omega$  and 4.8 M $\Omega$ .

Figure 3 shows the mechanism of generation triboelectricity in the TENG-based touch sensor developed in this work, similar to that proposed in [1, 34] for vertical contact-separation mode TENG-based on periodic contact and release of two dielectric layers connected with their own electrodes. As seen in Fig. 3, stage (I) corresponds to compression by an external mechanical force, when the distance  $d_3$  between two triboelectric layers PET and ZnO is reduced to zero. Since two dielectric materials are pressed against each other, due to the difference in electron affinity, contact electrification leads to the appearance of opposite static charges on the inner surfaces of PET and ZnO. Thus, the PET surface becomes negatively charged, while the zinc oxide surface becomes equally positively charged. When the external force is removed (at the releasing stage (II)), the density of the induced surface charge on the surfaces of PET and ZnO is equal to  $\sigma_m$  calculated by Eq. (4). Due to electrostatic induction, a potential difference  $U$  is created between ITO and CF, which, without external circuit, is equal to the open-circuit voltage  $UV = UV_{\text{oc}}$  given by Eq. (2), where  $d = d_1 + d_2 + d_3$ . At the same time, as can be seen

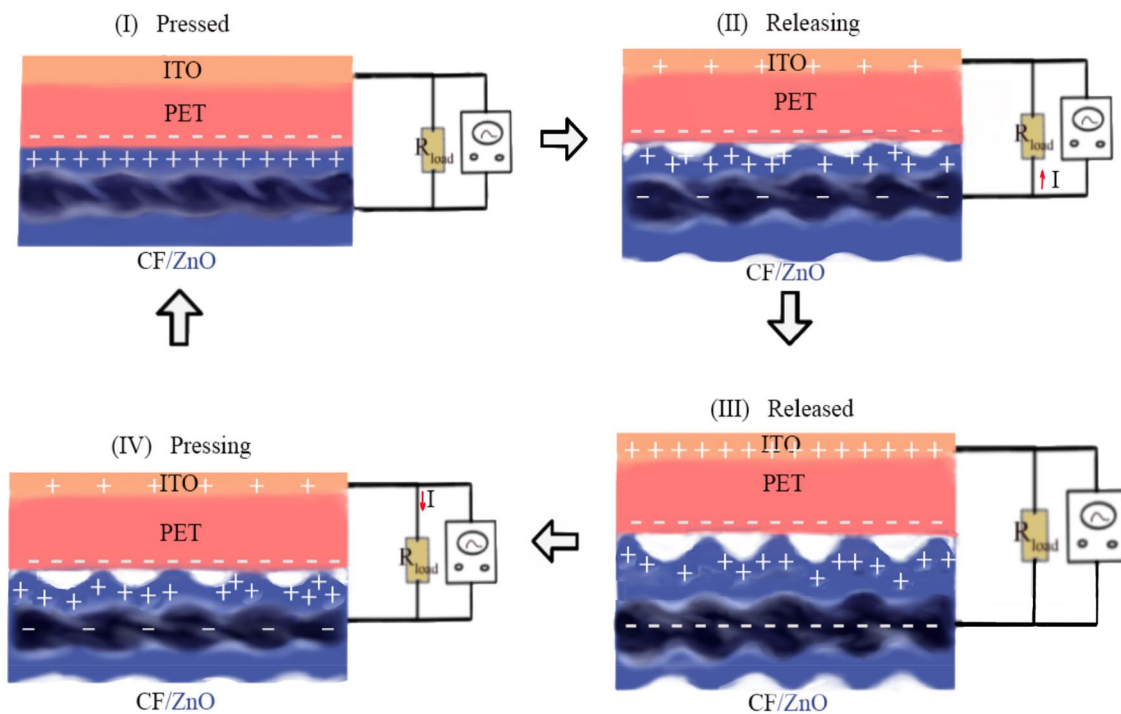


**Fig. 3** Schematic illustration of the operation principle of the self-powered wearable touch TES with the composition CF/ZnO/PET/ITO developed in this work

from Fig. 3, at stage (ii), the resulting potential difference will cause the electrons to flow through the external circuit under short current conditions or if the external load resistance  $R$  is not very high. Thus, this device will work as a weak strain sensor or a touch sensor, registering a pulsed current  $I$  through the load  $R$ , respectively. At the stage (III), an equilibrium of charges in the released layers has been reached, so there is no current in the external circuit. Once the pressing force is applied again, the potential difference between ITO and CF will decrease because PET and ZnO get closer to each other, and the electrostatic field disappears. As a result, in accordance with [31],  $UV_{oc}$  drops depending on the deformation depth  $\Delta h$  from the maximum value to zero when a full contact of the triboelectric surfaces is made again (i.e., when  $\Delta h = d_3$ ) according to the formula [31]:

$$V_{oc(\Delta h)} = \frac{\sigma(d_3 - \Delta h)}{\epsilon_0} \quad (5)$$

This process corresponds to the opposite direction of the current pulse, as shown in the pressing stage (IV) in Fig. 3. The opposite pulsed current is proportional to the pressure and can also be used in the TENG-based touch sensor. Thus, with periodic tapping, a TENG-based touch sensor with the composition CF/ZnO/PET/ITO generates an alternating current pulses at the output due to the triboelectrification and electrostatic induction. Through iterative process presented in Fig. 3, an alternative current power  $P$  is generated, which makes this sensor self-powered.

Herein, we tested two experimental samples of a flexible wearable TENG-based touch sensor based on a CF/ZnO/PET/ITO composition with an active area of  $2.5 \times 5$  cm, which differ from each other in the surface morphology and composition of nanostructured ZnO layers fabricated by the SILAR method with or without seed layers. With periodic gentle touch or tapping by hand with a small force ( $\sim 5$  N) and a low frequency in the range of 1.3–13 Hz, the signals of the prototypes of TENG-based touch sensor, such as open-circuit voltage  $UV_{oc}$ , output voltage  $UV$  and current density  $J$  at a certain external load resistance  $R$  were recorded. The value of  $J$  calculated as the current  $I$  at a certain  $R$  divided by the effective contact area  $A$  (i.e.,  $J = I/A$ ). When tested,  $A$  was  $1.5 \text{ cm}^2$ , so that the hand-touch pressure was about 33 kPa. In accordance with [5, 7], the instantaneous power density  $P$  of the sensors at a certain load resistance  $R$  was calculated as:

$$P = \frac{I^2 \cdot R}{A} \quad (6)$$

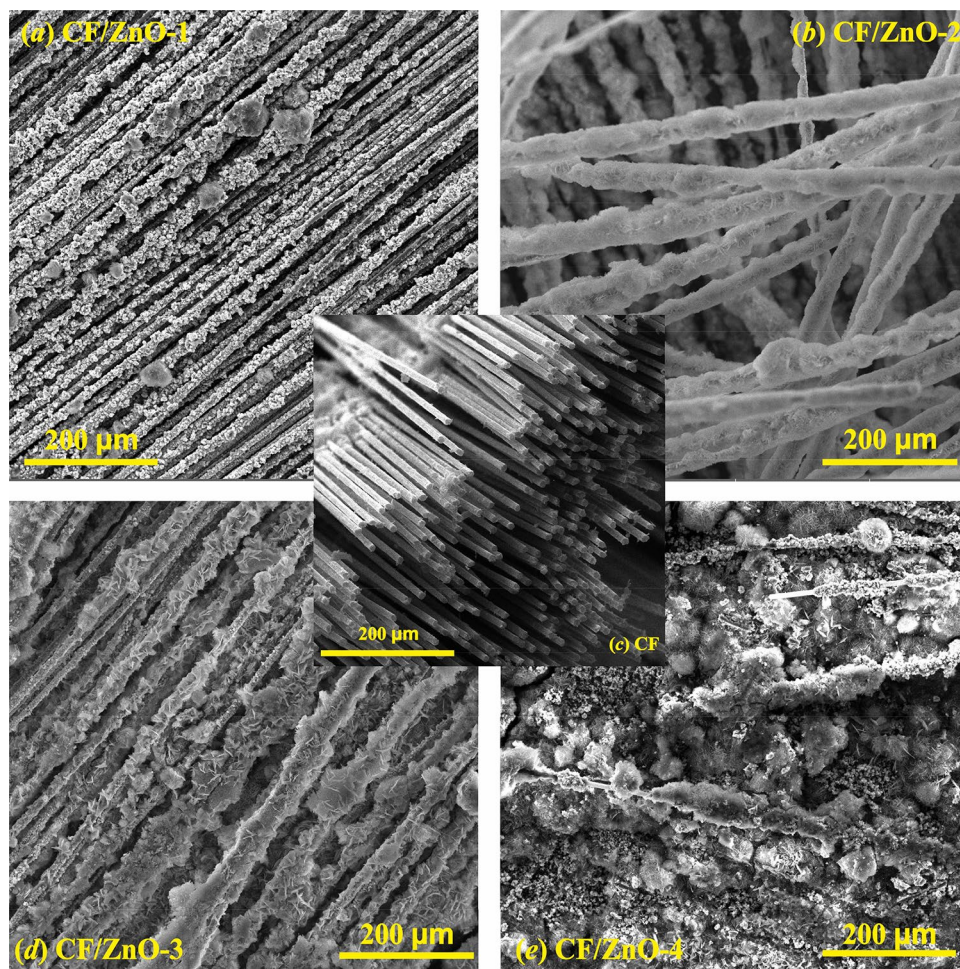
According to [1], the open-circuit voltage is determined only by the final configuration of the TENG-based sensor after applying a mechanical triggering, so that  $UV_{oc}$  is a measure of the magnitude of the strain and, thus, is related to the design of the sensor. At the same time, the output current depends on the rate at which the induced charge would flow, so the current signal is more sensitive to the dynamic process of how the mechanical pressure is applied [1, 30]. In connection with the foregoing, a TENG-based touch sensor can be used as a dual-mode one with recognition of the hardness of objects by analyzing the shape of current peaks [30, 35]. For the same applied force, the harder the object, the smaller the deformation region and, as a result, the sharper current peak is observed. For a soft material, the deformation is created gradually and over a longer time, which leads to a slow and steady accumulation and neutralization of the charge due to touch [30]. According to this mechanism, the hardness of an object can be determined from the width of the current peak (namely, from its FWHM) [30]. Since the integration of the area under the current peak corresponds to the charge  $Q$  transferred per pulse, in addition, in accordance with [7], as a parameter of the hardness of the object to which the sensor was pressed by hand, we used the peak area on the plot of  $I$  versus  $t$ . Therefore, herein, current signals of touch TES with the composition CF/ZnO/PET/ITO were recorded at various  $R$  for three materials with different hardness: glass, wood, and styrofoam. To do this, 5 mm thick plates made of the above materials were placed under the touch sensor, and the output currents were recorded during periodic tapping with a force of  $\sim 5$  N and a frequency of 1.3 Hz.

### 3 Results and discussion

The hydrophobic nature of carbon explains the more uniform coating of the surface of CF fibers with zinc oxide layers by the SILAR method, if these fibers were previously coated with ZnO seed layers. SEM images in Fig. 4a and b show the smoothed surfaces of the zinc oxide layers in the CF/ZnO-1 and CF/ZnO-2 samples, respectively. These samples differ in the thickness of the zinc oxide layer. Nevertheless, their SEM images taken at higher magnification in Fig. 5a and b,



**Fig. 4** SEM images taken at lower magnification: **a** CF/ZnO-1 sample with thinner ZnO layer fabricated by the SILAR method on the surface of CF fibers pre-coated with ZnO seed layers; **b** CF/ZnO-2 sample with thicker ZnO layer fabricated by the SILAR method on the surface of CF fibers pre-coated with ZnO seed layers; **c** fibers of uncoated carbon fabric; **d** CF/ZnO-3 sample with a thinner layer of ZnO fabricated by the SILAR method on the uncoated carbon fabric; **e** CF/ZnO-4 sample with thicker ZnO layer fabricated by the SILAR method on the uncoated carbon fabric



respectively, show that the zinc oxide layers both in the CF/ZnO-1 and CF/ZnO-2 samples are formed from multidirectional intergrown short ZnO nanorods with rounded ends.

In the case of zinc oxide deposition by the SILAR method directly on the hydrophobic surface of carbon fibers (CF/ZnO-3 and CF/ZnO-4 samples), we observed the growth by the SILAR method of standing nanosheets of zinc oxide with the basal plane (0002) of the hexagonal wurtzite structure and an unique *a*-axis texture. In other words, the growth of zinc oxide nanosheets was carried out in the direction perpendicular to the carbon fiber surface. The morphology of ZnO nanosheets is shown in Fig. 4d and e and in Fig. 5c and d. These interconnected ZnO nanosheets are strongly bonded to each other and are able to hold the CF carbon fibers together. The thickness of the nanosheets is about 100–200 nm in the thinner ZnO layer of the CF/ZnO-3 sample, while in the thicker ZnO layer of the CF/ZnO-4 sample, the thickness of

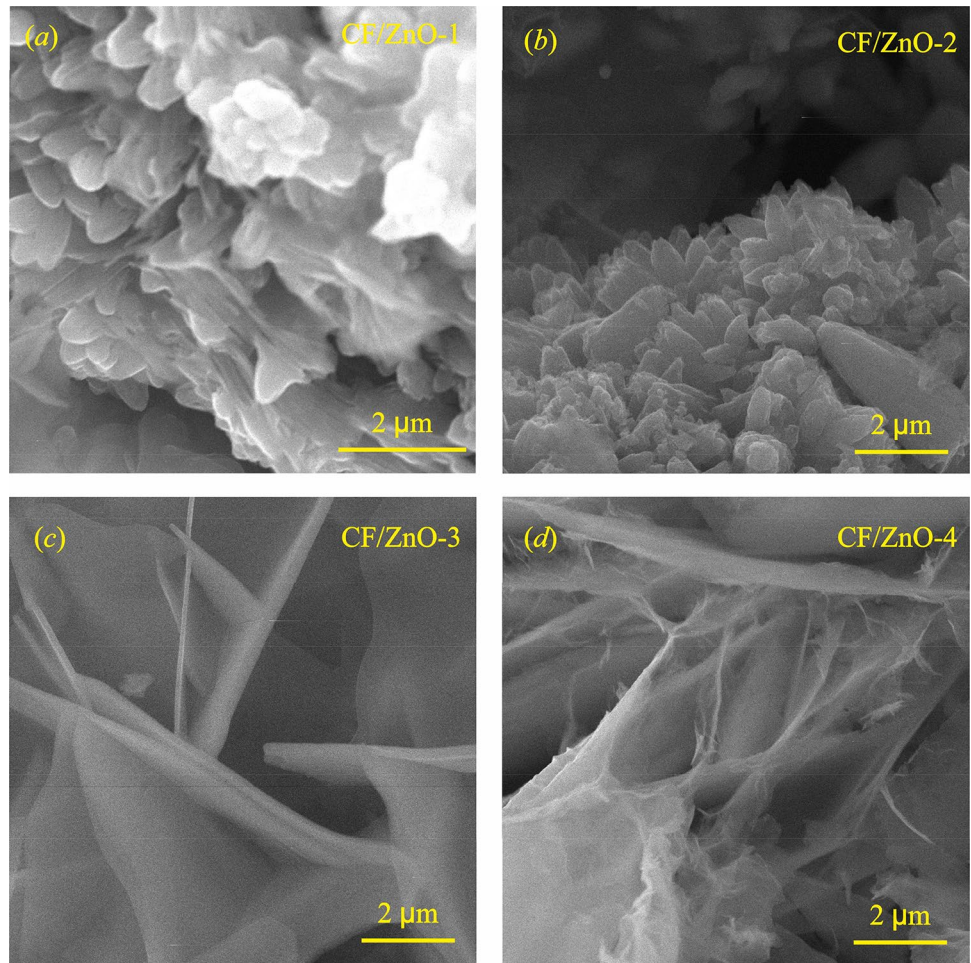
the nanosheets is about 50–100 nm. The width of the nanosheets ranges from 400 nm to 5 μm due to the spatial constraint.

Figure 6 shows SEM images of cross-sections of CF/ZnO-2 (a) and CF/ZnO-4 (c) samples and uncoated carbon fibers at appropriate magnifications (b) and (d), respectively, which makes it possible to compare the thicknesses of nanostructured ZnO layers made from multidirectional intergrown short nanorods with rounded ends in Fig. 6a and from interconnected nanosheets in Fig. 6b.

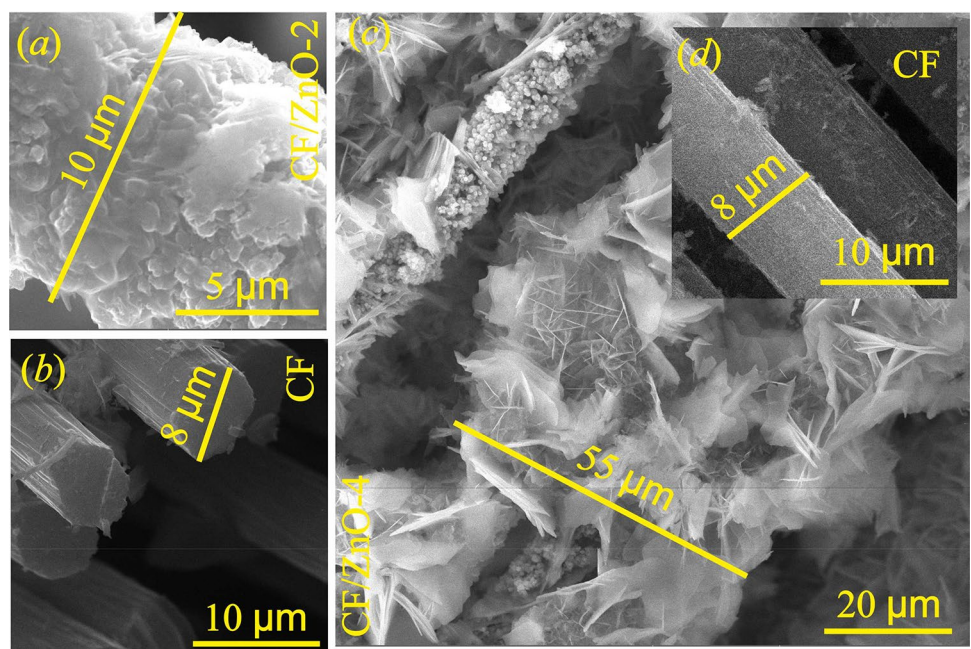
Figure 6a shows that the zinc oxide layer, which was grown by the SILAR method on the CF fibers pre-coated with ZnO seed layers, not only has a smooth surface, but also a rather dense morphology. The average thickness of the zinc oxide layer in the CF/ZnO-2 sample is about 1 μm. At the same time, if nanostructured ZnO layer was fabricated by the SILAR method on the bare carbon fabric, the obtained CF/ZnO-4 sample with interconnected ZnO nanosheets was ~ 20



**Fig. 5** SEM images taken at higher magnification: **a** CF/ZnO-1 sample with thinner ZnO layer fabricated by the SILAR method on the surface of CF fibers pre-coated with ZnO seed layers; **b** CF/ZnO-2 sample with thicker ZnO layer fabricated by the SILAR method on the surface of CF fibers pre-coated with ZnO seed layers; **c** CF/ZnO-3 sample with thinner layer of ZnO fabricated by the SILAR method on the bare carbon fabric; **d** CF/ZnO-4 sample with thicker ZnO layer fabricated by the SILAR method on the bare carbon fabric



**Fig. 6** SEM images with dimensions of CF/ZnO-2 (**a**) and CF/ZnO-4 (**c**) samples and uncoated carbon fibers in (**b**) and (**d**)



μm thick and very loose (Fig. 6c). According to [36], piezoelectric properties of layers of ZnO nanosheets can significantly enhance power density of TENG due to the high charge density induced by the polarization of ZnO nanosheets under the compressive force.

Figure 7 presents the experimental Raman spectra for two samples with ZnO layers deposited on the carbon fabric by the SILAR method with seed layers (CF/ZnO-2) (a) and without seed layers (CF/ZnO-4) (b). Table 1 summarizes the experimental data on the Raman signal intensity, its half-width, and the position of the Raman shift compared to the literature values for Raman active phonons in both bulk ZnO single crystal and thin polycrystalline ZnO films, according to [21, 25, 26, 38]. When analyzing the Raman spectra, it was taken into account that the crystal structure of wurtzite ZnO belongs to the hexagonal system with the space group  $C_{6v}^4 (P6_3mc)$  with two formula units per primitive cell, where all atoms occupy the positions  $C_{3v}$  [20, 22, 24, 25, 37]. Structure of wurtzite ZnO unit cell consists of four atoms, so there are 12 phonon branches in the crystal: 3 acoustic modes and 9 optical modes (3 longitudinal optical (LO) and 6 transverse optical (TO)) [26]. According to group theory, the active Raman phonons are  $A_1$  (z direction),  $E_1$  (xy direction), and two  $E_2$ . Inactive (silent) Raman phonons are  $B_1$  [20, 22, 24–26]. The characteristic Raman features for ZnO of this symmetry are non polarized  $E_{2(low)}$  and  $E_{2(high)}$  phonon modes at about  $101\text{ cm}^{-1}$  and  $437\text{ cm}^{-1}$ , respectively. Because of the strong occurrence of  $E_2$  modes in standard backscattering experiments, they are considered as a Raman fingerprint for ZnO [21, 23, 37]. As can be seen from Table 1; Fig. 7, these characteristic of the hexagonal structure peaks were observed in bulk ZnO crystals, as well as in both ZnO thin films with different morphologies deposited by the SILAR method in this work. According to [21], the low frequency  $E_{2(low)}$  mode is associated with the vibration of the heavy Zn sublattice, while the high frequency  $E_{2(high)}$  mode involves only the oxygen atoms. In literature [21, 38], the second order vibrations  $2E_{2(low)}$  in ZnO films appeared at about  $208\text{ cm}^{-1}$ . As it seen in Table 1; Fig. 7, in both samples CF/ZnO-2 and CF/ZnO-4, the positions of the  $E_{2(high)}$  and  $2E_{2(low)}$  modes as such as the  $E_{2(low)}$  mode in CF/ZnO-4 are blue shifted in comparison with the values of bulk ZnO and of ZnO films presented in [21, 38]. According to [21, 25], the observed for samples CF/ZnO-2 and CF/ZnO-4 small shifts of the optical phonon energy towards the high wavenumber side can suggest that

**Table 1** Experimental data on the intensity of the Raman signals, their half-widths, and the positions of the Raman peaks for ZnO films deposited by the SILAR method on the CF fabric with and without seed layers, in comparison with the literature data [21, 25, 26, 38] for the Raman active phonons of bulk ZnO single crystals and thin polycrystalline ZnO films

Optical mode	Sample	CF/ZnO-2			CF/ZnO-4			Peak position for bulk ZnO in [21], $\text{cm}^{-1}$	Peak position for bulk ZnO in [25], $\text{cm}^{-1}$
		Peak position, $\text{cm}^{-1}$	Intensity, arb. u.	FWHM, $\text{cm}^{-1}$	Peak position, $\text{cm}^{-1}$	Intensity, arb. u.	FWHM, $\text{cm}^{-1}$		
$E_{2(low)}$	100	25	23	106	12	25	101	101	
$E_{2(high)}$	444	26	20	448	15	18	437	437	
$A_1(\text{TO})$	-	-	-	-	-	-	380	380	
$A_1(\text{LO})$	-	-	-	-	-	-	574	574	
$E_1(\text{TO})$	398	38	23	401	25	21	407	407	
$E_1(\text{LO})$	611	17	35	614	11	24	583	583	
$2E_{2(low)}$	214	25	22	216 blue shift	20	24	208 thin film in [38]	208 thin film in [21]	
$A_1(\text{2LO})$	1136	12	52	1107	10	74	1100 thin film in [26]		

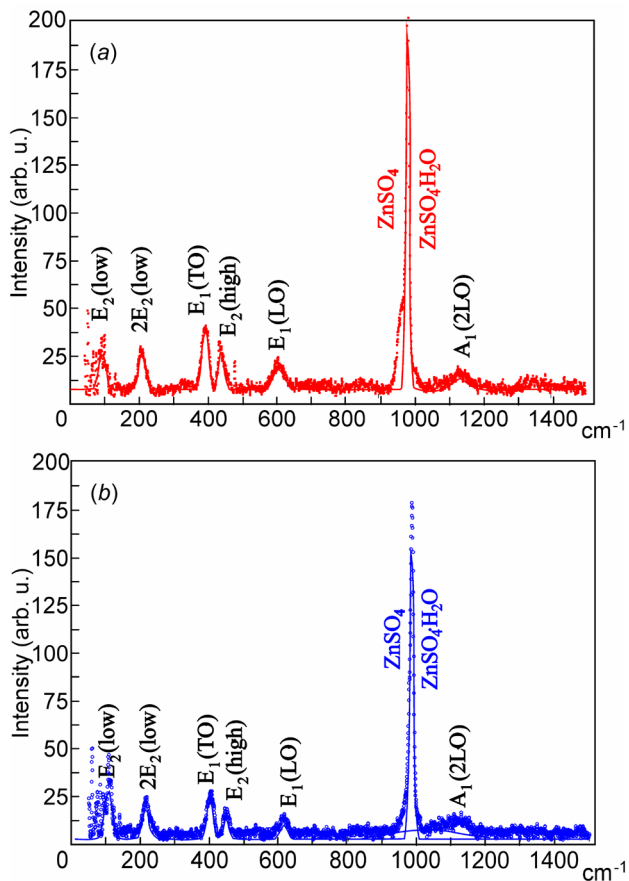


**Fig. 7** Raman spectra of ZnO films deposited by the SILAR method on the CF fabric with seed (a) and without seed (b) layers and excited with the 532 nm diode solid-state green laser line at room temperature

the deposited via SILAR nanostructured films have a bulk phonon structure rather than nanoparticle one. In accordance with [20, 22], the observed blue shifts of  $E_{2(\text{high})}$  Raman peaks are indicative of a compressive built-in stress in the zinc oxide films. In addition, in the CF/ZnO-4 sample prepared without a seed layer and consisting of the array of interconnected ZnO nanosheets, the intensity of the  $E_{2(\text{high})}$  peak is lower, similar to the  $2E_{2(\text{low})}$  and  $E_{2(\text{low})}$  peaks, which arise due to oxygen vibrations, indicating the presence of oxygen defects such as  $V_{\text{O}}$  vacancies [22].

According to the literature data [21, 26], the polarized  $E_1$  modes originate from oscillations of the two rigid sublattices and spread perpendicularly to the  $c$ -axis of ZnO. As it seen in Table 1; Fig. 7, both CF/ZnO-2 and CF/ZnO-4 samples have longitudinal and transverse components of  $E_1$  phonons,  $E_1(\text{LO})$  and  $E_1(\text{TO})$ , respectively. The position of  $E_1(\text{LO})$  mode

in both samples is blue shifted. As stated in [37], the  $E_1(\text{LO})$  peaks observed in the nanostructured ZnO layers prepared by the SILAR method in this work are attributed to the formation of the defects, such as oxygen vacancies and interstitial Zn, and also to the free carrier lack. On the contrary, the broadened  $E_1(\text{TO})$  peaks in both the CF/ZnO-2 and CF/ZnO-4 samples are slightly redshifted, apparently due to the nanoscale morphology of ZnO films, which is in good agreement with the data of [22]. The intensity of the  $E_1(\text{LO})$  and  $E_1(\text{TO})$  peaks is lower for the CF/ZnO-4 sample containing an array of interconnected ZnO nanosheets.

We did not detect polarized phonons  $A_1(\text{TO})$  and  $A_1(\text{LO})$  for both CF/ZnO-2 and CF/ZnO-4 samples prepared by the SILAR method. In a backscattering geometry, the  $A_1$  modes originate from oscillations of the two rigid sublattices and spread parallel to the  $c$ -axis of ZnO. Thus, in accordance with [26], the presence of  $A_1(\text{LO})$  mode strongly points the crystallization of ZnO with the  $c$ -plane as a growth-plane. As shown by SEM studies (Figs. 3, 4 and 5), the preferential orientation in the [0001] direction is not characteristic of either the CF/ZnO-2 sample or the CF/ZnO-4 sample. In addition, the absence of the  $A_1(\text{LO})$  mode in the Raman spectra in Fig. 7 can be explained according to [22] by its high sensitivity to lattice defects, such as oxygen vacancies. At the same time, the Raman spectra of both CF/ZnO-2 and CF/ZnO-4 samples in Fig. 7 show low broad peaks of second order vibrations  $A_1(2\text{LO})$  at wavenumbers around  $1100 \text{ cm}^{-1}$ .

Strong Raman peaks observed for both CF/ZnO-2 and CF/ZnO-4 samples at wavenumbers  $\sim 1000 \text{ cm}^{-1}$ , in accordance with [39], belong to zinc sulfate impurities, such as a mixture of gunningite ( $\text{ZnSO}_4 \cdot \text{H}_2\text{O}$ ) and anhydrous  $\text{ZnSO}_4$  (zincosite), appeared from cationic precursor solution used in the SILAR deposition. It is important to note that during the study, neither shift and broadening, nor change in the intensity of the Raman peaks due to local heating under the action of a laser beam was observed, which means that both CF/ZnO-2 and CF/ZnO-4 samples of triboelectric textiles are thermally stable.

The EDS spectra and corresponding EDS maps of the CF/ZnO-2 and CF/ZnO-4 samples in Fig. 8 and data Table 2 confirm the presence of sulfur in the elemental composition of both samples. The layer in the form of interconnected zinc oxide nanosheets in CF/ZnO-4 contains a particularly large amount of sulfur, which is explained by its especially large specific



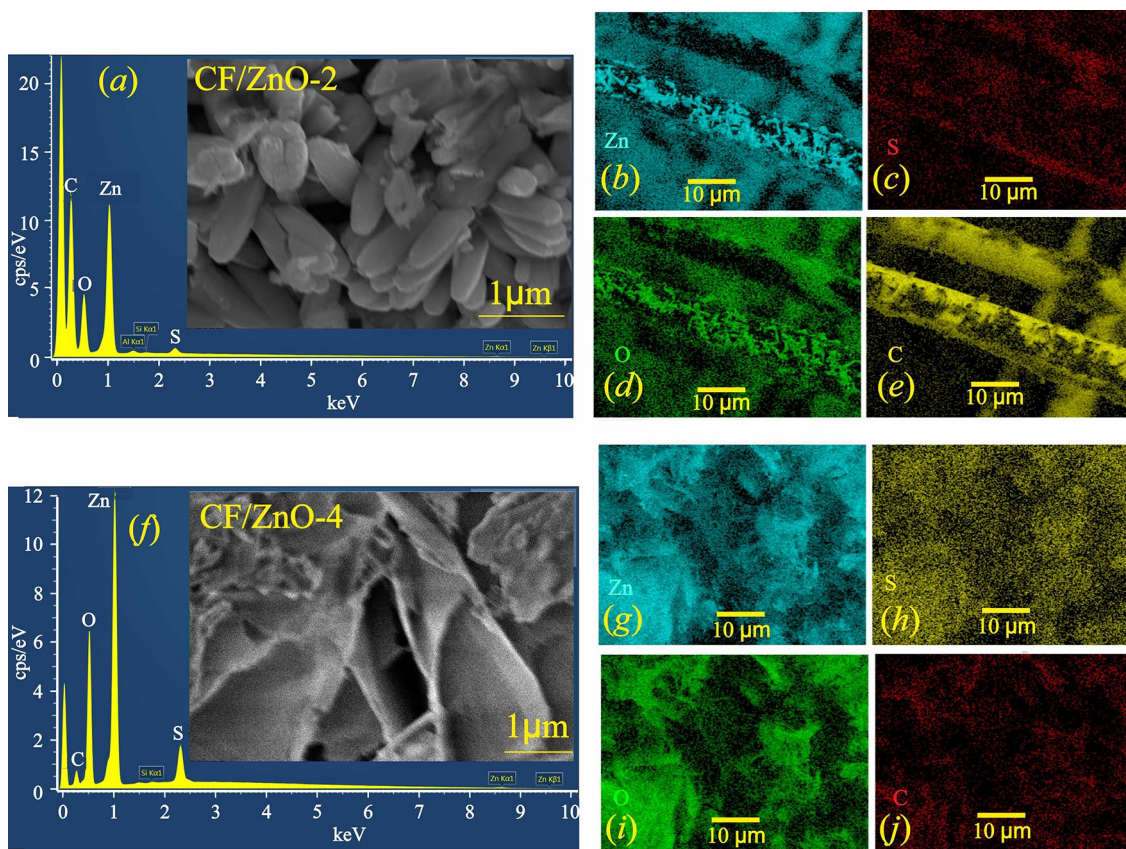


**Fig. 8** Elemental composition of CF/ZnO-2 sample in (a), (b), (c), (d), (e) and CF/ZnO-4 sample in (f), (g), (h), (i), (j); a and f EDS spectra with corresponding high-resolution SEM images

**Table 2** Elemental composition of the CF/ZnO-2 sample with ~ 1 μm thick ZnO layer obtained by the SILAR method on the surface of CF fibers pre-coated with ZnO seed layers and the CF/ZnO-4 sample with ~ 20 μm thick ZnO nanosheet film fabricated by the SILAR method on bare CF

Sample	Composition according to EDS, at%			
	Zn	O	S	C
CF/ZnO-2	9	16	1	74
CF/ZnO-4	27	46	8	19

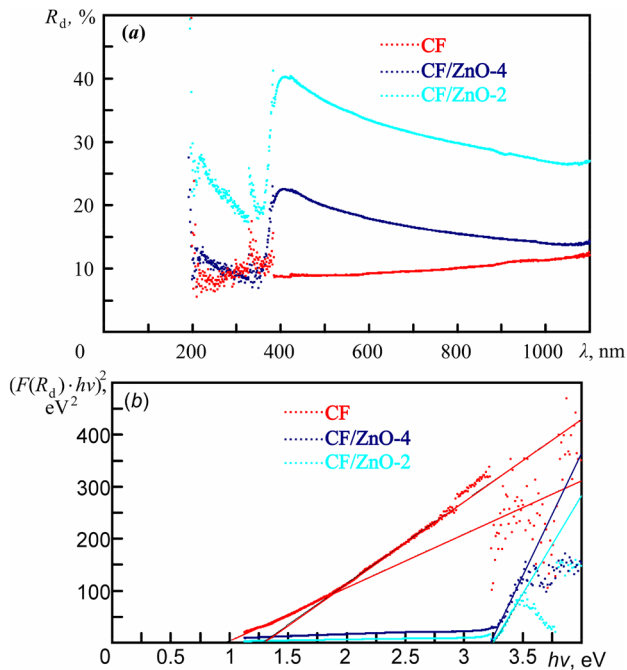
surface area. In addition, according to Fig. 8; Table 2, we can conclude that this nanosheet layer in the CF/ZnO-4 sample contains significantly more zinc oxide than the layer of intergrown nanorods in the CF/ZnO-2 sample, which agrees well with the SEM data in Fig. 6.

Figure 9 shows significant diffuse optical reflections of nanostructured layers of direct-gap semiconductor ZnO films and their optical band gap of 3.25 eV,

in insets; b and g EDS maps of zinc; c and h EDS maps of sulphur; d and i EDS maps of oxygen; e and j EDS maps of carbon

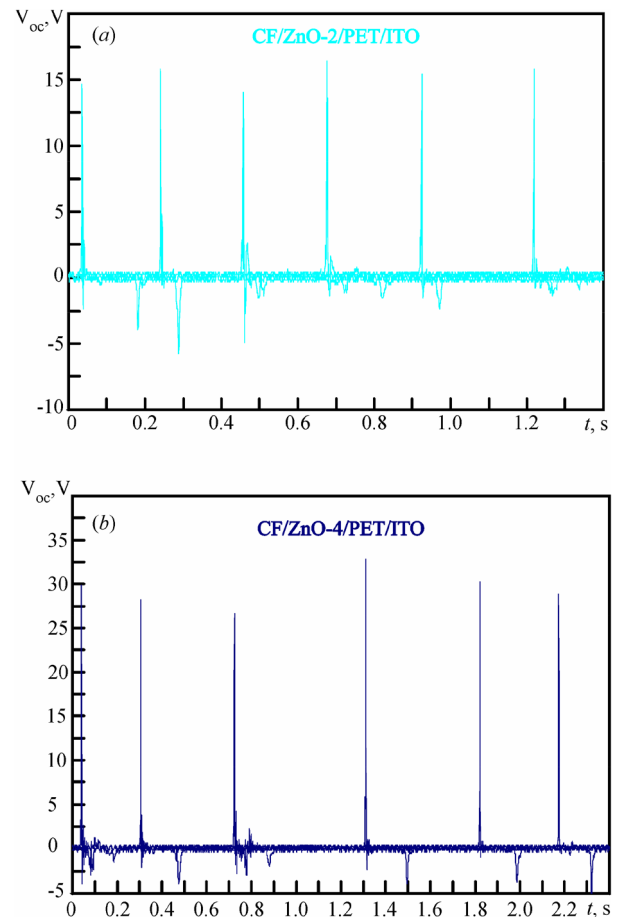
which is close to the typical value of  $E_g = 3.37$  eV for this material [17, 33, 40]. According to [40], the exciton Bohr radius of ZnO is about 0.9 nm. Therefore, the absence of an increase in  $E_g$  due to the quantum confinement effect indicates that the sizes of ZnO crystals in the CF/ZnO-2 and CF/ZnO-4 samples significantly exceed this value, which is in good agreement with the results of Raman spectroscopy. High values of  $R_d$  up to 22% for interconnected nanosheets and up to 42% for multidirectional intergrown short ZnO nanorods with rounded ends are in good agreement with the morphology and thickness of the nanostructured ZnO layers.

Figure 10 shows real-time open-circuit voltage pulses, which are a response to repeated hand tapping with a pressure of ~ 33 kPa, for two experimental samples of flexible wearable TENG-based touch sensors with CF/ZnO/PET/ITO composition, namely for CF/ZnO-2/PET/ITO and CF/ZnO-4/PET/ITO samples. When testing, the sensors were placed



**Fig. 9** Optical properties of CF/ZnO-2 and CF/ZnO-4 triboelectric textile samples with nanostructured ZnO layers of different morphology on the surface of carbon fibers, and optical properties of uncoated carbon fabric: **a** diffuse reflectance spectra  $R_d(\lambda)$ ; **b** graphs to determine the band gap of ZnO using the Kubelka–Munk function

on the wooden surface of the table. It can be seen that the reaction of the sensors to a touch by hand is almost instantaneous, the voltage pulses are high and extremely sharp, and their duration is a few milliseconds. As it was preliminarily experimentally shown, in a narrow low frequency range of 1.3–13 Hz, there was no change in the open-circuit voltage  $UV_{oc}$  (at the pressed stage (I) of the TENG operation) depending on the frequency. The touch sensor with the tribopositive textile part CF/ZnO-2 has shown an average open-circuit voltage of  $\sim 15$  V (Fig. 10a). At the same time, the sensor with the tribopositive CF/ZnO-4 textile made on the layer of interconnected zinc oxide nanosheets produced a higher  $UV_{oc}$  value of  $\sim 30$  V (Fig. 10b). The reverse voltage pulses corresponding to the released stage (III) of the TENG operation differed in Fig. 10 from each other both in magnitude and in time, depending on the duration of pressing and the features of tapping with a hand on the TENG-based sensor. This property of triboelectric sensors with CF/ZnO/PET/ITO composition can be further used to identify objects touching their surface, like fingerprints.



**Fig. 10** Open-circuit voltages for two experimental samples of flexible wearable TENG-based touch sensors with CF/ZnO/PET/ITO composition upon repeated tapping by hand with a pressure  $\sim 33$  kPa

Calculations by Eqs. (2) and (4) have revealed that due to nanosheet morphology of ZnO layer the maximum induced by the touching surface charge density  $\sigma_m$  for triboelectric textile CF/ZnO-4 ( $\sigma_m = 0.7 \mu\text{C}/\text{m}^2$ ) almost double the value for CF/ZnO-2 ( $\sigma_m = 0.4 \mu\text{C}/\text{m}^2$ ).

The output signals obtained at various external load resistances  $R$  for the developed TENG-based touch sensors with periodic hand tapping on the sensors with a force of  $\sim 5$  N (with a pressure  $\sim 33$  kPa) are shown in Fig. 11. All output data, namely voltage and current density in Fig. 11a and power density in Fig. 11b, are better for the CF/ZnO-4/PET/ITO sensor sample, which has tribopositive CF/ZnO-4 textile with layer of ZnO nanosheets in its design.

The values of electrical output parameters obtained in this study for TES CF/ZnO-4/PET/ITO with carbon

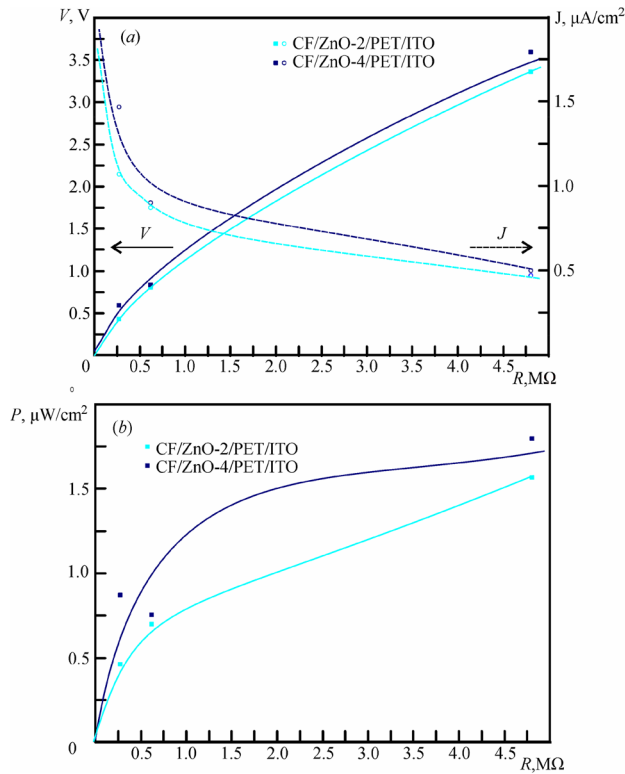


**Fig. 11** Electrical output performance of two developed experimental samples of flexible wearable TENG-based touch sensors with CF/ZnO/PET/ITO composition at a compressive force of Fig. 10 shows real-time open-circuit voltage pulses, which are responses to repeated hand tapping with  $\sim 5$  N (at pressure of  $\sim 33$  kPa) depending on various external load resistances  $R$ : **a** voltage  $UV$  and current density  $J$ ; **b** – output power density  $P$

fabric coated with ZnO nanosheet grids, shown in Table 3, are comparable or exceed modern data for wearable triboelectric nanogenerators in the form of fibers, yarns and textile [4], and for triboelectric nanogenerators based on ZnO nanostructures [41]. Moreover, the output characteristics of triboelectric and piezoelectric nanogenerators and sensors given in review [42] for future soft robots and machines confirm the promise of the development presented here.

To recognize the hardness of objects by analyzing the shape of the current peaks, in accordance with [30, 35], two experimental samples of the TENG-based CF/ZnO/PET/ITO touch sensor were placed on plates 5 mm thick made of glass, wood, or styrofoam. Figure 12 shows some typical shapes of the single pulses of the output currents of these TESs in real-time, recorded in external circuits with different load resistances in response to tapping with an applied force of  $\sim 5$  N (pressure  $\sim 33$  kPa). In Fig. 12, the peaks obtained during testing with the location of the CF/ZnO-2/PET/ITO and CF/ZnO-4/PET/ITO sensors on the hard wooden plate are highlighted with light olive shading. As can be seen in Fig. 12, the sharpest peaks were obtained when hard glass or wood plates was placed under the sensor, and the broadest peaks were recorded when the sensors were placed on soft styrofoam plate. Considering the rather large spread of results, to calculate the full width at half maximum of the current peak and the charge  $Q$  transferred per pulse, each measurement was repeated twenty times, the averaged data on the FWHM and  $Q$  are given in Table 3. From Table 3 it can be seen that the material of the plate under the TES affects the charge transferred per pulse and the width of the current peak: the softer the material, the

**Table 3** Electrical characteristics of two developed experimental samples of flexible wearable touch TES with the composition CF/ZnO/PET/ITO on the surface of soft and hard plates at

a compressive force of  $\sim 5$  N (at a pressure of  $\sim 33$  kPa) caused by repeated tapping with a hand with a frequency in the range of 1.3–13 Hz

TES sample	Material of the plate under the TES	Electrical parameters of TES					
		FWHM, ms (at $R=0.27$ M $\Omega$ )	Charge transferred in one pulse $Q$ , $\mu\text{C}$ (at $R=0.27$ M $\Omega$ )	Open-circuit voltage $UV_{oc}$ , V	Output voltage $UV$ , V (at $R=4.8$ M $\Omega$ )	Current density $J$ , $\mu\text{A}/\text{cm}^2$ (at $R=0.27$ M $\Omega$ )	Power density $P$ , $\mu\text{W}/\text{cm}^2$ (at $R=4.8$ M $\Omega$ )
CF/ZnO-2/PET/ITO	Glass	1.81	2.54	$\sim 15$	3.36	1.07	1.57
	Wood	1.89	3.26				
	Styrofoam	3.36	4.03				
CF/ZnO-4/PET/ITO	Glass	1.56	3.29	$\sim 30$	3.60	1.47	1.80
	Wood	1.84	3.58				
	Styrofoam	2.36	3.68				



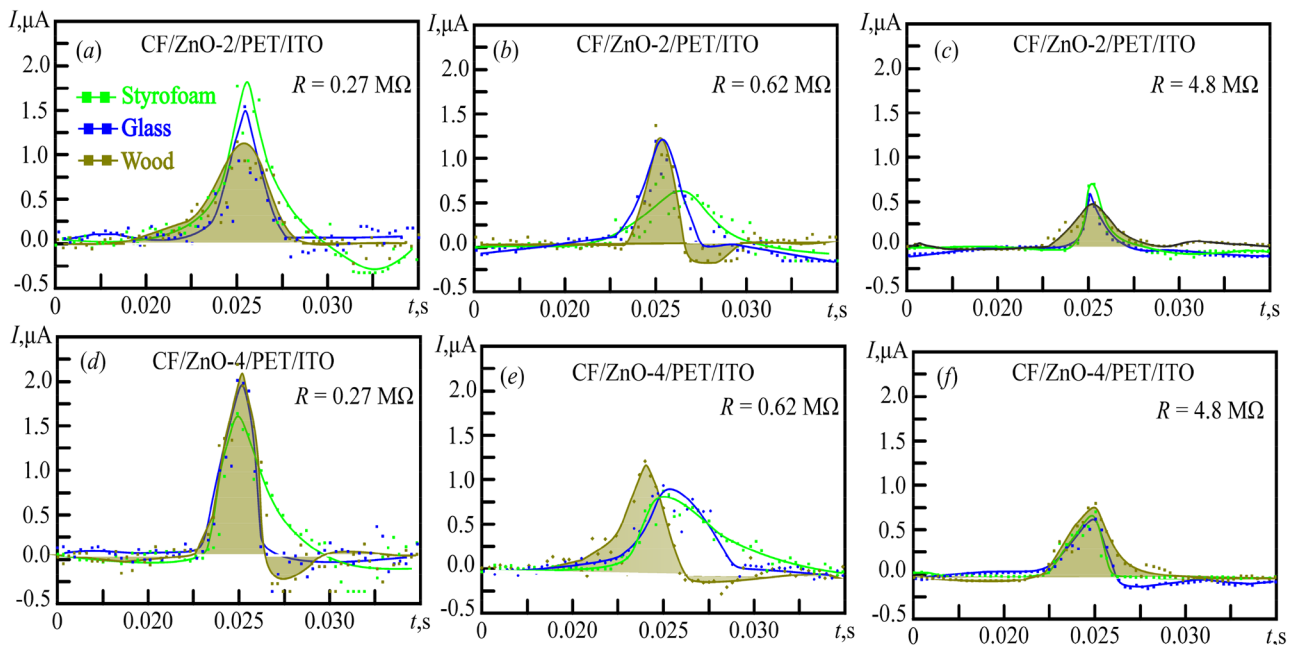


**Fig. 12** Graphs of  $I$  versus  $t$  showing single current pulses of two TENG-based touch sensors placed on glass, wood, or styrofoam plates, recorded at various load resistances  $R$  in response to tapping with an applied force of  $\sim 5$  N ( $\sim 33$  kPa pressure)

greater the  $Q$  and the higher the FWHM. Thus, both TENG-based touch sensors developed in this work can be used as dual-mode sensors due to the ability to recognize the hardness of objects.

## 4 Conclusions

In this work, the automatic SILAR method, depending on the deposition mode, made it possible to create triboelectric CF/ZnO textile materials with different morphology and properties. Rather uniform coating of CF with multidirectionally intergrown short ZnO nanorods with rounded ends was obtained if the carbon fibers were preliminarily coated with ZnO seed layers. However, when the ZnO layer was fabricated by the SILAR method on bare carbon fabric, we obtained arrays of ZnO nanosheets strongly bonded to each other. As visualized by SEM images, the thickness of the nanosheets is in the range of 50–200 nm, their width varies from 400 nm to 5  $\mu$ m due to spatial constraints. The Raman spectra confirmed the hexagonal wurtzite crystal structure of both types of ZnO layers and the unique  $a$ -axis texture of zinc oxide nanosheets standing in the direction perpendicular to the carbon fiber surface. Both types of ZnO layers contain defects such as oxygen vacancies. In addition, the layers of

ZnO in the form of interconnected nanosheets contain a large amount of sulfur from the solution used in the SILAR method, which is explained by the especially large specific surface area of the nanosheet grids. During the Raman study, neither shift and broadening, nor change in the intensity of the Raman peaks due to local heating under the action of the laser beam was observed, which means that the CF/ZnO triboelectric fabrics are thermally stable. Both types of CF/ZnO textiles exhibit significant diffuse optical reflections, which is in good agreement with the morphology and thickness of nanostructured ZnO layers, and have a direct optical band gap of 3.25 eV, close to that of bulk zinc oxide.

As a proof-of-concept, we designed and tested two prototypes of flexible TENG-based touch sensors of vertical contact-separation mode that differ in the type of nanostructured ZnO layer. Due to textile-specific advantages such as high surface roughness and elasticity, the developed sensors with CF/ZnO/PET/ITO compositions and active areas of  $2.5 \times 5$  cm do not require specially designed separators or springs between the triboelectric layers, since a gap is involuntarily formed between the smooth layer PET and woven carbon textiles coated with nanostructured ZnO films. When tested with repeated hand tapping at a low frequency of 1.3–13 Hz, and with a force of  $\sim 5$  N (pressure of



~ 33 kPa), triboelectric sensors with intergrown short ZnO nanorods and with ZnO nanosheet grids demonstrate open-circuit voltage pulses  $UV_{oc} \approx 15$  V and  $UV_{oc} \approx 30$  V, respectively. These pulses are extremely sharp, their duration does not exceed a few milliseconds. Due to the nanosheet morphology of the ZnO layer, the maximum touch-induced surface charge density for the corresponding triboelectric textile ( $\sigma_m = 0.7 \mu\text{C}/\text{m}^2$ ) is almost two times higher than for the CF/ZnO textile with intergrown short ZnO nanorods ( $\sigma_m = 0.4 \mu\text{C}/\text{m}^2$ ). During testing, the TENG-based touch sensor with interconnected ZnO nanosheets showed a higher efficiency: an output voltage of 3.6 V, a current density of  $1.47 \mu\text{A}/\text{cm}^2$ , and a power density of  $1.8 \mu\text{W}/\text{cm}^2$ . These results are comparable or superior to current data for wearable triboelectric nanogenerators in the form of fibers, yarns and textiles, as well as for TENG-based on ZnO nanostructures designed for future soft robots and human-machine interfaces. Moreover, both TENG-based sensors developed in this work can be used as dual-mode sensors due to the ability to recognize the hardness of objects such as glass, wood and styrofoam by analyzing the shape of the output current peaks. The sharpest peaks were obtained when hard glass plates were placed under the sensor, and the widest peaks were recorded when the sensors were placed on the soft styrofoam plate. The softer the material, the wider the current peak and the larger its area corresponding to the charge transferred per pulse. Thus, the new design of the flexible triboelectric sensor based on carbon fabric coated with nanostructured zinc oxide layers developed in this work combines the advantages of autonomy, availability of materials, simple design, low-cost and ease of manufacture with high output characteristics and versatility.

## Acknowledgements

The authors are grateful to the Ministry of Education and Science of Ukraine and the MSCA4Ukraine consortium funded under the EU Maria Skłodowska-Curie Program for ensuring the implementation of the work. In addition, we are grateful to Martin Stuchlik, Junior researcher, Department of Nanochemistry, Institute of Nanomaterials, Advanced Technologies and Innovation, Technical University of Liberec, for Raman spectroscopy studies and advice on Raman spectra description.

## Author contributions

All authors contributed to the study conception and design. The first draft of the manuscript was written by N.P. Klochko and all authors commented on previous versions of the manuscript. S.I. Petrushenko: Investigation, Conceptualization, Methodology, Formal analysis. Validation. M. Fijalkowski: Material preparation, Methodology, Formal analysis. V.R. Kopach: Methodology, Validation, Writing—review & editing. Y.M. Shepotko: Investigation, Writing—review & editing. K. Adach: Methodology, Investigation, Writing—review & editing. A. Fedonenko: Methodology, Investigation, Visualization. S.V. Dukarov: Investigation, Writing—review & editing. V.M. Sukhov: Data collection and analysis. Writing—review & editing. A.L. Khrypunova: Visualization, Writing—review & editing. N.P. Klochko: Conceptualization, Methodology, Validation, Writing—original draft. All authors read and approved the final manuscript.”

## Funding

Open access publishing supported by the National Technical Library in Prague. The work was supported by the Ministry of Education and Science of Ukraine and within the MSCA4Ukraine project funded by the European Union. Views and opinions expressed are however, the those of the author(s) only and do not necessarily reflect the views of the European Union. Neither the European Union, nor the MSCA4Ukraine Consortium as a whole, nor individual member institutions of the MSCA4Ukraine Consortium can be held responsible for them.

## Data availability

The data that support the findings of this study are available from the corresponding author, S.I. Petrushenko, upon reasonable request.

## Declarations

**Conflict of interest** The authors have no relevant financial or non-financial interests to disclose.

**Open Access** This article is licensed under a Creative Commons Attribution 4.0 International License, which permits use, sharing, adaptation, distribution and reproduction in any medium or format, as long as you give appropriate credit to the original author(s) and the source, provide a link to the Creative Commons licence, and indicate if changes were made. The images or other third party material in this article are included in the article's Creative Commons licence, unless indicated otherwise in a credit line to the material. If material is not included in the article's Creative Commons licence and your intended use is not permitted by statutory regulation or exceeds the permitted use, you will need to obtain permission directly from the copyright holder. To view a copy of this licence, visit <http://creativecommons.org/licenses/by/4.0/>.

## References

1. Z.L. Wang, Triboelectric nanogenerators as new energy technology for self-powered systems and as active mechanical and chemical sensors. *ACS Nano*. **7**(11), 9533–9557 (2013). <https://doi.org/10.1021/nn404614z>
2. W.-G. Kim, D.-W. Kim, I.-W. Tcho, J.-K. Kim, M.-S. Kim, Y.-K. Choi, Triboelectric nanogenerator: structure, mechanism, and applications. *ACS Nano*. **15**, 258–287 (2021). <https://doi.org/10.1021/acsnano.0c09803>
3. R. Cheng, K. Dong, L. Liu, C. Ning, P. Chen, X. Peng, D. Liu, Z.L. Wang, Flame-retardant textile-based triboelectric nanogenerators for fire protection applications. *ACS Nano*. **14**(11), 15853–15863 (2020). <https://doi.org/10.1021/acsnano.0c07148>
4. J. Xiong, P.S. Lee, Progress on wearable triboelectric nanogenerators in shapes of fiber, yarn, and textile. *Sci. Technol. Adv. Mater.* **20**(1), 837–857 (2019). <https://doi.org/10.1080/14686996.2019.1650396>
5. Z. Bai, Y. Xu, J. Li, J. Zhu, C. Gao, Y. Zhang, J. Wang, J. Guo, An eco-friendly porous nanocomposite fabric-based triboelectric nanogenerator for efficient energy harvesting and motion sensing. *ACS Appl. Mater. Interfaces*. **12**, 42880–42890 (2020). <https://doi.org/10.1021/acsnano.0c12709>
6. B. Baro, S. Khimhun, U. Das, S. Bayan, ZnO based triboelectric nanogenerator on textile platform for wearable sweat sensing application. *Nano Energy* **108**, 108212–108211 (2023)
7. J. Yi, K. Dong, S. Shen, Y. Jiang, X. Peng, C. Ye, Z.L. Wang, Fully fabric-based triboelectric nanogenerators as self-powered human–machine interactive keyboards. *Nano-Micro Lett.* **13**, 103 (2021). <https://doi.org/10.1007/s40820-021-00621-7>
8. W. Seung, M.K. Gupta, K.Y. Lee, K.-S. Shin, J.-H. Lee, T.Y. Kim, S. Kim, J. Lin, J.H. Kim, S.W. Kim, Nanopatterned textile-based wearable triboelectric nanogenerator. *ACS Nano* **9**(4), 3501–3509 (2015). <https://doi.org/10.1021/nn507221f>
9. J. Liu, L. Gu, N. Cui, Q. Xu, Y. Qin, R. Yang, Fabric-based triboelectric nanogenerators. *Research* (2019). <https://doi.org/10.34133/2019/1091632>
10. R. Walden, I. Aazem, A. Babu, S.C. Pillai, Textile-triboelectric nanogenerators (T-TENGs) for wearable energy harvesting devices. *Chem. Eng. J.* (2023). <https://doi.org/10.1016/j.cej.2022.138741>
11. J. Xiong, P. Cui, X.C.J. Wang, K. Parida, M.-F. Lin, P.S. Lee, Skin-touch-actuated textile-based triboelectric nanogenerator with black phosphorus for durable biomechanical energy harvesting. *Nat. Commun.* (2018). <https://doi.org/10.1038/s41467-018-06759-0>
12. P. Huang, D.-L. Wen, Y. Qiu, M.-H. Yang, C. Tu, H.-S. Zhong, X.S. Zhang, Textile-based triboelectric nanogenerators for wearable self-powered microsystems. *Micromachines* **12**, 158–151 (2021). <https://doi.org/10.3390/mi12020158>
13. S. Jung, J. Lee, T. Hyeon, M. Lee, D.-H. Kim, Fabric-based integrated energy devices for wearable activity monitors. *Adv. Mater.* **26**(36), 6329–6334 (2014). <https://doi.org/10.1002/adma.201402439>
14. Y.P. Lim, J.S.C. Koay, J.T. Zhao, S. Huang, B.T. Goh, K.C. Aw, B. Chen, C.Y. Haw, W.C. Gan, Modulating ZnO growth structures for maximum power output of hybrid piezo/triboelectric nanogenerator. *Adv. Funct. Mater.* (2022). <https://doi.org/10.1002/adfm.202206750>
15. J. Wang, B. Weng, P.L.Y. Liu, Synthesis of ZnO nanoarrays on carbon fibers using combined atomic layer deposition and hydrothermal methods. *Mater. Res. Express* (2018). <https://doi.org/10.1088/2053-1591/aac845>
16. F. Xie, W. Hu, D.N.L. Zhuo, J. Deng, Z. Lu, ZnO nanowires decoration on carbon fiber via hydrothermal synthesis for paper-based friction materials with improved friction and wear properties. *Ceram. Int.* **44**(4), 4204–4210 (2018). <https://doi.org/10.1002/adma.201402439>
17. Q. Abbas, M.S. Javed, A. Ahmad, S.H. Siyal, I. Asim, R. Luque, M.D. Albaqami, A.M. Tighezza, ZnO nano-flowers assembled on carbon fiber textile for high-performance supercapacitor's electrode. *Coatings*. **11**, 1337 (2021). <https://doi.org/10.3390/coatings11111337>
18. Y. Du, C. Fu, Y. Gao, L. Liu, Y. Liu, L. Xing, F. Zhao, Carbon fibers/ZnO nanowires hybrid nanogenerator based on

- an insulating interface barrier. *RSC Adv.* **7**, 21452–21458 (2017). <https://doi.org/10.1039/c7ra02491f>
19. J. Fei, D. Luo, J. Huang, C. Zhang, X. Duan, Growth of aligned ZnO nanorods on carbon fabric and its composite for superior mechanical and tribological performance. *Surf. Coat. Technol.* **344**, 433–440 (2018). <https://doi.org/10.1016/j.surfcoat.2018.03.056>
  20. K. Tapily, D. Gu, H. Baumgart, M. Rigo, J. Seo, Raman spectroscopy of ZnO thin films by atomic layer deposition. *ECS Trans.* **33**(2), 117–123 (2010). <https://doi.org/10.1149/1.3485248>
  21. M. Koyano, P. Quoc Bao, L. thi Thanh Binh, L. Hong Ha, N. Ngoc Long, Katayama Photoluminescence and Raman Spectra of ZnO thin films by charged liquid cluster beam technique. *Phys. Stat. Sol. (a)*. **193**(1), 125–131 (2002).
  22. T. Torchynska, B. El Filali, J.A. Jaramillo Gomez, G. Polupan, J.L. Ramírez García, L. Shcherbyna, Raman scattering, emission, and deep defect evolution in ZnO:In thin films. *J. Vacuum Sci. Technol. A* (2020). <https://doi.org/10.1116/6.0000364>
  23. A.R. Ansari, S. Hussain, M. Imran, A.A. Al-Ghamdi, M.R. Chandan, Optical investigations of microwave induced synthesis of zinc oxide thin-film. *Mater. Science-Poland.* **36**(2), 304–309 (2018). <https://doi.org/10.1515/msp-2018-0041>
  24. F.K. Konan, B. Hartiti, A. Batan, B. Aka, X-ray diffraction, XPS, and raman spectroscopy of coated ZnO:Al (1–7 at%) nanoparticles. *Surf. Sci. Nanotechnol.* **17**, 163–168 (2019). <https://doi.org/10.1380/ejssnt.2019.163>
  25. B.E. Filali, T.V. Torchynska, A.I. Díaz Cano, M. Morales, Rodriguez, Structural and raman scattering studies of ZnO Cu nanocrystals grown by spray pyrolysis. *Revista Mexicana De Ingeniería Química.* **14**(3), 781–788 (2015). <http://www.redalyc.org/articulo.oa?id=62043088018>
  26. E. Nowak, W. Stachowiak, D. Koczorowski, K. Schulz, S. Fabisiak, Los, A comprehensive study of structural and optical properties of ZnO bulk crystals and polycrystalline films grown by sol–gel method. *Appl. Phys. A* (2020). <https://doi.org/10.1007/s00339-020-03711-2>
  27. M. Patel, A. Chavda, I. Mukhopadhyay, J. Kim, A. Ray, Nanostructured SnS with inherent anisotropic optical properties for high photoactivity. *Nanoscale.* **8**, 2293–2303 (2016). <https://doi.org/10.1039/c5nr06731f>
  28. J. Zeng, J. Zhao, C. Li, Y. Qi, G. Liu, X. Fu, H. Zhou, C. Zhang, Triboelectric nanogenerators as active tactile stimulators for multifunctional sensing and artificial synapses. *Sensors.* **22**, 975–971 (2022). <https://doi.org/10.3390/s22030975>
  29. H. Varghese, H.M.A. Hakkeem, M. Farman, E. Thouti, S. Pillai, A. Chandran, Self-powered flexible triboelectric touch sensor based on micro-pyramidal PDMS films and cellulose acetate nanofibers. *Results Eng.* (2022). <https://doi.org/10.1016/j.rineng.2022.100550>
  30. T. Li, J. Zou, F. Xing, M. Zhang, X. Cao, N. Wang, Wang, From dual-mode triboelectric nanogenerator to smart tactile sensor: a multiplexing design. *ACS Nano.* **11**(4), 3950–3956 (2017). <https://doi.org/10.1021/acsnano.7b00396>
  31. K.Y. Lee, H.-J. Yoon, T. Jiang, X. Wen, W. Seung, S.-W. Kim, Z.L. Wang, Fully packaged self-powered triboelectric pressure sensor using hemispheres-array. *Adv. Energy Mater.* (2016). <https://doi.org/10.1002/aenm.201502566>
  32. M. Ma, Z. Zhang, Z. Zhao, Q. Liao, Z. Kang, F. Gao, X. Zhao, Y. Zhang, Self-powered flexible antibacterial tactile sensor based on triboelectric-piezoelectric-pyroelectric multi-effect coupling mechanism. *Nano Energy* (2019). <https://doi.org/10.1016/j.nanoen.2019.104105>
  33. D. Kaur, A. Bharti, T. Sharma, C. Madhu, Dielectric properties of ZnO-based nanocomposites and their potential applications. *Int. J. Opt.* (2021). <https://doi.org/10.1155/2021/9950202>
  34. Y. Wang, Y. Yang, Z.L. Wang, Triboelectric nanogenerators as flexible power sources. *Flex. Electron.* (2017). <https://doi.org/10.1038/s41528-017-0007-8>
  35. Y. Cheng, D. Wu, S. Hao, Y. Jie, X. Cao, N. Wang, Z.L. Wang, Highly stretchable triboelectric tactile sensor for electronic skin. *Nano Energy.* **64**, 103907 (2019). <https://doi.org/10.1016/j.nanoen.2019.103907>
  36. A.A. Narasimulu, P. Zhao, N. Soin, K. Prashanthi, P. Ding, J. Chen, S. Dong, L. Chen, E. Zhou, C.D. Montemagno, Luo, Significant triboelectric enhancement using interfacial piezoelectric ZnO nanosheet layer. *Nano Energy.* **40**, 471–480 (2017). <https://doi.org/10.1016/j.nanoen.2017.08.053>
  37. D. Gültekin, H. Akbulut, Raman studies of ZnO products synthesized by solution based methods. *Acta Phys. Pol., a* **129**(4), 803–805 (2016). <https://doi.org/10.12693/APhysPolA.129.803>
  38. M. Wang, L. Jiang, E.J. Kim, S.H. Hahn, Electronic structure and optical properties of Zn(OH)<sub>2</sub>:LDA + U calculations and intense yellow luminescence. *RSC Adv.* (2015). <https://doi.org/10.1039/c5ra17024a>
  39. W.W. Rudolph, M.H. Brooker, P.R. Tremaine, Raman spectroscopy of aqueous ZnSO<sub>4</sub> solutions under hydrothermal conditions: solubility, hydrolysis, and sulfate ion pairing. *J. Solution Chem.* **28**, 621–630 (1999). <https://doi.org/10.1023/A:1022691117630>
  40. P. Singh, R.K. Singh, R. Kumar, Journey of ZnO quantum dots from undoped to rare-earth and transition metal-doped

- and their applications. *RSC Adv.* **11**, 2512–2545 (2021). <https://doi.org/10.1039/D0RA08670C>
41. P. Supraja, R.R. Kumar, S. Mishra, D. Haranath, P.R. Sankar, K. Prakash, N. Jayarambabu, T.V. Rao, K.U. Kumar, A simple and low-cost triboelectric nanogenerator based on two dimensional ZnO nanosheets and its application in portable electronics. *Sens. Actuators: Phys.* **335**, 113368 (2022). <https://doi.org/10.1016/j.sna.2022.113368>. -1-113368-11
42. M. Pan, C. Yuan, X. Liang, J. Zou, Y. Zhang, C. Bowen, Triboelectric and piezoelectric nanogenerators for future soft robots and machines. *iScience* (2020). <https://doi.org/10.1016/j.isci.2020.101682>

**Publisher's Note** Springer Nature remains neutral with regard to jurisdictional claims in published maps and institutional affiliations.